



Photocatalytic reduction of Cr(VI) on WO₃ doped long TiO₂ nanotube arrays in the presence of citric acid

Lixia Yang^{a,b,c}, Yan Xiao^{a,b}, Shaohuan Liu^c, Yue Li^c, Qingyun Cai^c, Shenglian Luo^{a,b,c,d,*}, Guangming Zeng^{a,b}

^a College of Environmental Science and Engineering, Hunan University, Changsha 410082, PR China

^b Key Laboratory of Environmental Biology and Pollution Control, Ministry of Education, Hunan University, Changsha 410082, PR China

^c State Key Laboratory of Chemo/Biosensing and Chemometrics, Hunan University, Changsha 410082, PR China

^d School of Environment and Chemical Engineering, Nanchang Hangkong University, Nanchang 330063, PR China

ARTICLE INFO

Article history:

Received 27 July 2009

Received in revised form 28 October 2009

Accepted 3 November 2009

Available online 10 November 2009

Keywords:

WO₃

TiO₂ nanotube arrays

Cr(VI)

Photocatalytic reduction

ABSTRACT

Photoreduction of Cr(VI) was successfully achieved on WO₃ doped TiO₂ nanotube (NT) arrays in the presence of citric acid. WO₃ doped TiO₂ NT arrays were fabricated by annealing anodic titania NTs that were preloaded with peroxotungstic acid. Driven by electrostatic force, the negatively charged peroxotungstic acid sol uniformly clung to the positively charged titania NT arrays, causing a solid solution of WO₃ and TiO₂ after annealing. The citric acid plays an important role in the photoreduction of Cr(VI): (i) it works as a sacrificial electron donor to deplete the photogenerated holes from the excited TiO₂; and (ii) it takes part in the redox with Cr(VI) under UV illumination because of its electron rich property. The photochemical-reduction rate of Cr(VI) in citric acid under simulated solar light was 6.9 μg/L min cm². Subtracting the part mentioned above, the reduction rate of Cr(VI) due to photogenerated electrons from excited photocatalysts increased from 8.3 μg/L min cm² on TiO₂ NTs to 31.6 μg/L min cm² on WO₃/TiO₂ NTs containing 1 at% of W. The net Cr(VI) reduction rate on WO₃/TiO₂ NT arrays is 3.76 times that on the unmodified TiO₂ NTs. Since both WO₃ and TiO₂ can be excited by UV light, the enhanced photoactivity of WO₃/TiO₂ is attributed to the increased probability of charge-carrier separation and the extended photo-response spectrum in visible light region due to the doping of WO₃ (band gap: 2.6 eV).

© 2009 Elsevier B.V. All rights reserved.

1. Introduction

Hexavalent chromium (Cr(VI)) contamination in natural waters is a serious global environmental problem that can have serious toxic effects on human health. The main source of anthropogenic chromium pollution in ground water are plating industries, cooling towers, leather tanning, wood preservation and steel manufacturing [1,2]. In general, the techniques employed for the removal of Cr(VI) are chemical precipitation, reverse osmosis, ion exchange, foam flotation, electrolysis, adsorption, and photocatalytic reduction [3,4]. Among the present methods, photocatalysis by applying TiO₂ is an efficient, active, and clean technology for Cr(VI) reduction in aqueous media in view of solar energy conversion. The highly toxic, carcinogenic, and mobile Cr(VI) can be photo-reduced to the less harmful Cr(III), which can then be precipitated in neutral or alkaline solutions [5].

However, the application of TiO₂ is limited by its high band gap energy (3.2 eV), which diminishes its absorption in the visible light range of solar spectrum. Many efforts have been devoted to extending the spectral response of TiO₂ to the visible spectrum by doping with Cu, Fe, N [6–8] or narrow band gap semiconductors such as Fe₂O₃, CdSe, Cu₂O, Bi₂O₃ [9–11]. Tungsten oxide is a promising inorganic material exhibiting excellent electrochromic, photochromic, gasochromic and energy storage properties [12,13]. Because W⁶⁺ has an ionic radius similar to that of Ti⁴⁺, WO₃ can couple into TiO₂ crystals in their co-crystallization process during annealing, resulting in a well doped WO₃/TiO₂ composite [14]. Incorporating WO₃ with TiO₂ [15–20] not only efficiently inhibits the recombination between the photogenerated holes and electrons but also reduces the band gap of TiO₂. In comparison to undoped TiO₂, higher photocatalytic activities in photodegradation of gas-phase or liquid-phase organic pollutants have been achieved on WO₃ modified TiO₂ powders [15–17] or mesoporous WO₃/TiO₂ films [18–20], which can be ascribed to the optical absorption ability of WO₃ doped TiO₂ materials in higher wavelength region. However, the application of photocatalysts in powder form generally needs appropriate substrates to support

* Corresponding author at: State Key Laboratory of Chemo/Biosensing and Chemometrics, Hunan University, Changsha 410082, PR China.

E-mail address: slou@hnu.cn (S. Luo).

the catalysts or the filtration procedure after photocatalysis while the WO_3/TiO_2 films generally do not possess large surface area.

Consequently, our interests lie in the anodic titania NT arrays with controllable pore sizes, length, and high orientation. The precisely controllable dimensional features of the NT arrays and the oriented nature of the crystalline (after annealing in oxygen atmosphere) nanotubes provide excellent short diffusion path length for the electrons transfer as compared with the thin films, reducing bulk recombination of photogenerated electron–hole pairs [21,22].

TiO_2 NT arrays have proven useful in applications such as dye-sensitized solar cells, contamination removal, and photodegradation [23–27]. Because the TiO_2 NTs are grown from a Ti substrate, their integrality makes the practical application simpler and more cost-effective as compared with TiO_2 powders, avoiding the filtration step after photoreaction or the immobilizing process required for photocatalyst particles.

In the present study, WO_3 was doped in long TiO_2 NT arrays, constructing a composite photocatalysts for the photoreduction of Cr(VI) in the presence of citric acid which is a naturally occurring compound in plants and soils [28]. Citric acid served as the donor scavenger to deplete the photogenerated holes from TiO_2 -based catalysts, increasing the reduction rate of Cr(VI) as which prevented the reoxidation of chromium species by the holes or hydroxyl radicals [29].

By virtue of the high surface area, open pore structure with enhanced adsorption capacity, and increased photoactivity owing to the WO_3 doping, a fast reduction of Cr(VI) to Cr(III) was expected on the composite WO_3/TiO_2 NT arrays in the presence of citric acid.

2. Experimental

2.1. Preparation of WO_3/TiO_2 NT arrays

Titanium foils with a thickness of $127\ \mu\text{m}$ (99.8%; Sigma–Aldrich) were cleaned with acetone and ethanol prior to anodization. The foils ($4.5\ \text{cm} \times 1\ \text{cm}$) were subjected to potentiostatic anodization in a two-electrode configuration using a dc power supply with a platinum foil cathode. The titanium sample was only partially immersed in the electrolyte, with the upper un-anodized portion used as an electrical contact. The effective surface area of TiO_2 catalysts is $4\ \text{cm} \times 1\ \text{cm}$. The distance between anode and cathode was 2 cm. The titania NTs of $8\ \mu\text{m}$ length were obtained in a dimethyl sulfoxide (DMSO) solution containing 2 wt% hydrofluoric acid (HF) by treatment at 40 V for 12 h.

Peroxotungstic acid sol was prepared based on a modification of the route developed by Kudo [30]: 1 g metallic tungsten powder was added slowly to 20 mL of 30% H_2O_2 under agitation at $30\ ^\circ\text{C}$. After $\sim 2\ \text{h}$ stirring, the tungsten powders were almost completely dissolved, with only a slight residual white powder that was subsequently removed by filtration, leaving a clear peroxotungstic acid sol. To deplete the excess H_2O_2 and make the sol negatively charged, 20 mL of anhydrous ethanol was added to the sol under stirring. The as-anodized titania NTs were then immersed in the peroxotungstic acid sol for a specified duration, then the sol-containing titania NTs were annealed for crystallization at $550\ ^\circ\text{C}$ for 6 h in a tube furnace at a heating rate of $2\ ^\circ\text{C}/\text{min}$. In order to study the influence of WO_3 content on TiO_2 photoactivity, the NTs were immersed in the sol with four durations of 0.25, 0.5, 1 or 2 h. The WO_3 doped TiO_2 NT arrays were designated as $\text{W}_x\text{-TiO}_2$ NTs in this work, where x refers to the W atom percentage in the TiO_2 NTs.

2.2. Characterization of WO_3/TiO_2 NT arrays

The topology of the catalyst was characterized using a field-emission scanning electron microscope (FE-SEM) operating at 5 kV

(JSM 6700F; JEOL, Tokyo, Japan). Energy dispersive X-ray (EDX) spectrometers fitted to electron microscopes were used for elemental analysis. Transmission electron microscopy (TEM) images were obtained using a JEM 3010 (JEOL, Tokyo, Japan) operating at 300 kV. X-ray photoelectron spectroscopy (XPS) analyses of the specimen were carried out in an ultrahigh vacuum chamber with a pressure of 2×10^{-9} mbar at room temperature (Thermo Fisher Scientific, ESCALAB 250). The binding energy (BE) scale was calibrated by measuring a C 1s peak at 284.8 eV from the surface contamination. The resultant XPS spectra were simulated by assuming the photoelectron peaks to have a Gaussian line shape.

2.3. Optical determination and photocatalysis on WO_3/TiO_2 NT arrays

UV–vis absorption spectra of the specimens were recorded with a UV–vis spectrophotometer (Cary 300, USA) equipped with an integrating sphere with radius of 150 mm. The photoreduction of Cr(VI) was performed in a flowing configuration shown as Fig. 1. In order to illustrate the mechanism of photocatalytic reduction of Cr(VI) on WO_3/TiO_2 NTs, a Hg lamp and a Xe lamp (Beijing, Trustech. Co. Ltd.) were both used. The optimized concentration of citric acid in water samples was 24 mM with a pH value of 2 measured with a Delta 320 pH meter (pH 0.00–14.00 with a resolution of 0.01 pH, Mettler-Toledo, Shanghai, China). The light was passed through a water filter, which removed the infrared wavelengths to yield light at the photo-anode at a measured intensity of $25\ \text{mW}/\text{cm}^2$ for Hg lamp and $100\ \text{mW}/\text{cm}^2$ for Xe lamp, as determined by a NOVA Oriel 70260 with a thermodetector. After removing the IR irradiation, the photocatalytic reactions were performed at room temperature. A Cr(VI) solution of 20 mL with an initial concentration of 20 mg/L was circulated through a quartz tube exposed to the light in which were placed the WO_3/TiO_2 or undoped TiO_2 NT arrays of an effective geometrical size of $4\ \text{cm} \times 1\ \text{cm}$. After the photocatalytic experiment was initiated, 0.1 mL volumes of solution were periodically withdrawn from the reaction vessel, and the Cr(VI) concentrations were measured using the diphenylcarbazide (DPC) method at 540 nm, which effectively diminishes the interference from the absorption of citric acid and its degradation intermediates. Every experiment was repeated for 3 times for ensuring the reliability.

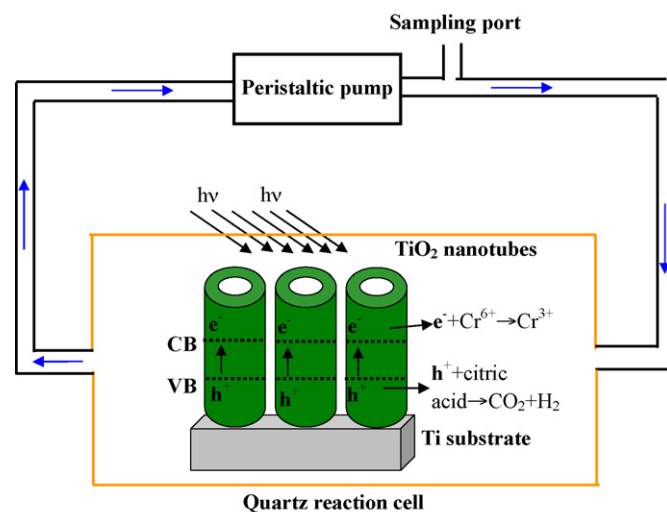


Fig. 1. Schematic illustration the process of the Cr(VI) photocatalytic reduction in the presence of citric acid under illumination. The blue arrows indicate the flow direction of the Cr(VI) –citric acid solution. (For interpretation of the references to color in this figure legend, the reader is referred to the web version of the article.)

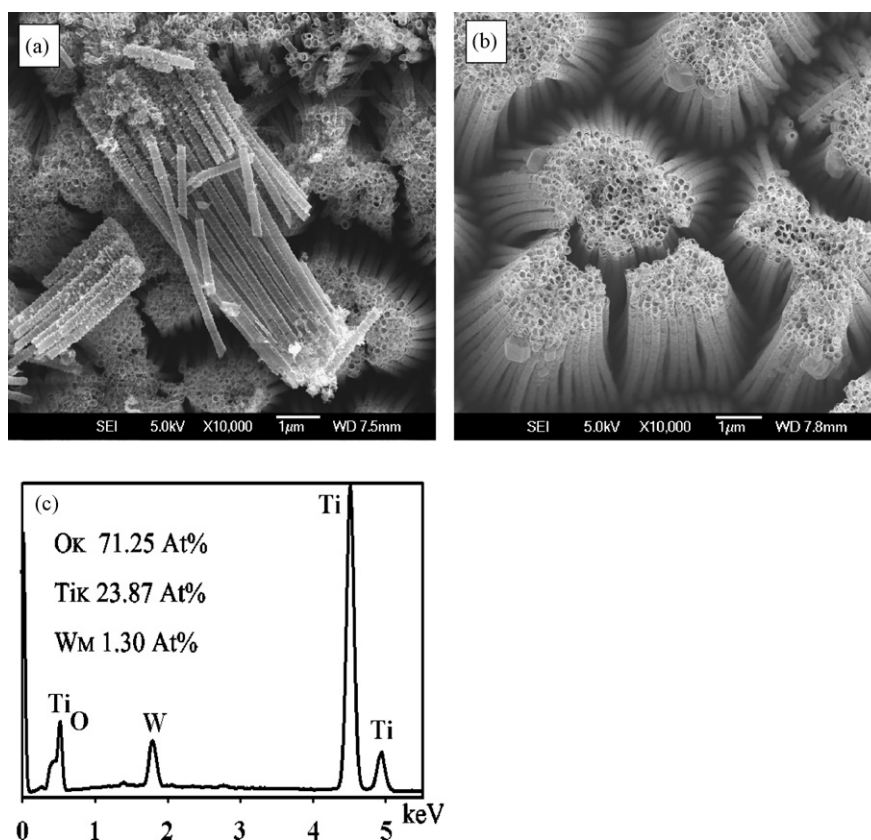


Fig. 2. (a) Topology of the as-fabricated amorphous titania nanotubes. The nanotubes are with 125 nm pore size, 8 μm length. (b) SEM image of $\text{W}_{1.3\text{at\%}}\text{-TiO}_2$ nanotubes annealed at 550 $^\circ\text{C}$ for 6 h. (c) EDS spectrum with inset elements analysis of the specimen.

3. Results and discussion

3.1. Characterization of the $\text{W}_x\text{-TiO}_2$ NT arrays

The SEM image of Fig. 2a shows that the TiO_2 NTs prepared in DMSO at 40 V for 12 h were 8 μm in length, 125 nm in pore size, and 15 nm in wall thickness. Fig. 2b shows the morphology of the calcined WO_3/TiO_2 NTs prepared by immersing the TiO_2 NTs in the peroxotungstic acid sol for 1 h. After annealing, the composite NTs still retained a high degree of orientation with open tops and did not lose their architecture, which is essential to a high photocatalytic activity. Fig. 2c shows the EDS spectrum of the WO_3/TiO_2 NTs, depicting that the W content is 1.3 at%.

In order to investigate the distribution of the WO_3 in TiO_2 NTs with increasing W content, four specimens with different W content ranging from 0.77 to 2.45 at% were prepared by immersing TiO_2 NTs in peroxotungstic acid sol for 0.25, 0.5, 1, and 2 h, respectively. The corresponding TEM images are given in Fig. 3. The NTs with W content ≤ 1.0 at% are almost transparent, as shown in Fig. 3a and b, indicating a good combination of WO_3 and with TiO_2 crystals. The similar ionic radii of W^{6+} and Ti^{4+} allow W^{6+} to easily dissolve into the TiO_2 lattice [14]. The high-resolution TEM image shown in Fig. 3c confirms that the WO_3/TiO_2 composite is composed of WO_3 and TiO_2 crystals in which clear 2-D lattice fringes can be seen. The fringe spacing of 0.352 nm corresponds to the (1 0 1) plane of anatase. The fringe spacing of 0.384 and 0.262 nm corresponds to the (0 0 2) and (2 0 2) planes of the triclinic WO_3 , respectively. The selected area electron diffraction pattern shown in Fig. 3d further confirms that the NT arrays are composed of TiO_2 and WO_3 multicrystals. However, the substitution of Ti^{4+} by tungsten ion has a limit over which tungsten ions cannot further substitute Ti^{4+} and these then assemble at the grain boundary interface, forming crystals there. As

shown in Fig. 3e, for the 1.3 at% W-containing TiO_2 NTs ($\text{W}_{1.3\text{at\%}}\text{-TiO}_2$ NTs), WO_3 particles can be clearly seen on the interior and exterior walls of the TiO_2 NTs. The corresponding EDX analysis of these particles given in Fig. 3f illustrates that the particles consist primarily of WO_3 . The number of WO_3 particles further increases in $\text{W}_{2.45\text{at\%}}\text{-TiO}_2$ NTs, as shown in Fig. 3g. The overloaded WO_3 particles filled in the TiO_2 NT, resulting in a decrease in the interior space of the photocatalyst.

XPS measurements were carried out to elucidate the surface chemical composition and oxidation state of the WO_3/TiO_2 NT arrays achieved by immersing TiO_2 NTs in peroxotungstic acid sol for 1, 2, and 4 h to give the final W content of 1.29, 2.39, 4.33 at%, respectively (Fig. 4). Since XPS spectroscopy is a more accurate detector, the W content determined by XPS spectroscopy are not strictly consistent with those determined by the EDX spectrometers. However, all of the data depict a trend that the W content increased several fold with increasing dipping time in peroxotungstic acid sol. As is shown in the high-resolution XPS of Ti 2p (Fig. 4a), the characteristic peak at 484.4 eV assigned to Ti^{4+} [31–33] shifted to higher binding energies with the increasing W contents. In Fig. 4b, the peak positions at 35.5 and 37.61 eV corresponding to W 4f_{7/2} and 4f_{5/2}, respectively, confirm the W^{6+} species [31,34]. Table 1 shows the detail information of XPS

Table 1
XPS analysis result for TiO_2 and WO_3/TiO_2 NT arrays.

Peaks	TiO_2	WO_3 [ref. 34,35]	1.29 at% W	2.39 at% W	4.33 at% W
Ti 2p _{3/2}	458.4		459.1	459.17	459.53
Ti 2p _{1/2}	464		465	465.1	465.4
Ti 3p			37.23	37.3	37.68
W 4f _{7/2}		35.5	35.54	35.66	36.02
W 4f _{5/2}		37.61	37.69	37.81	38.17

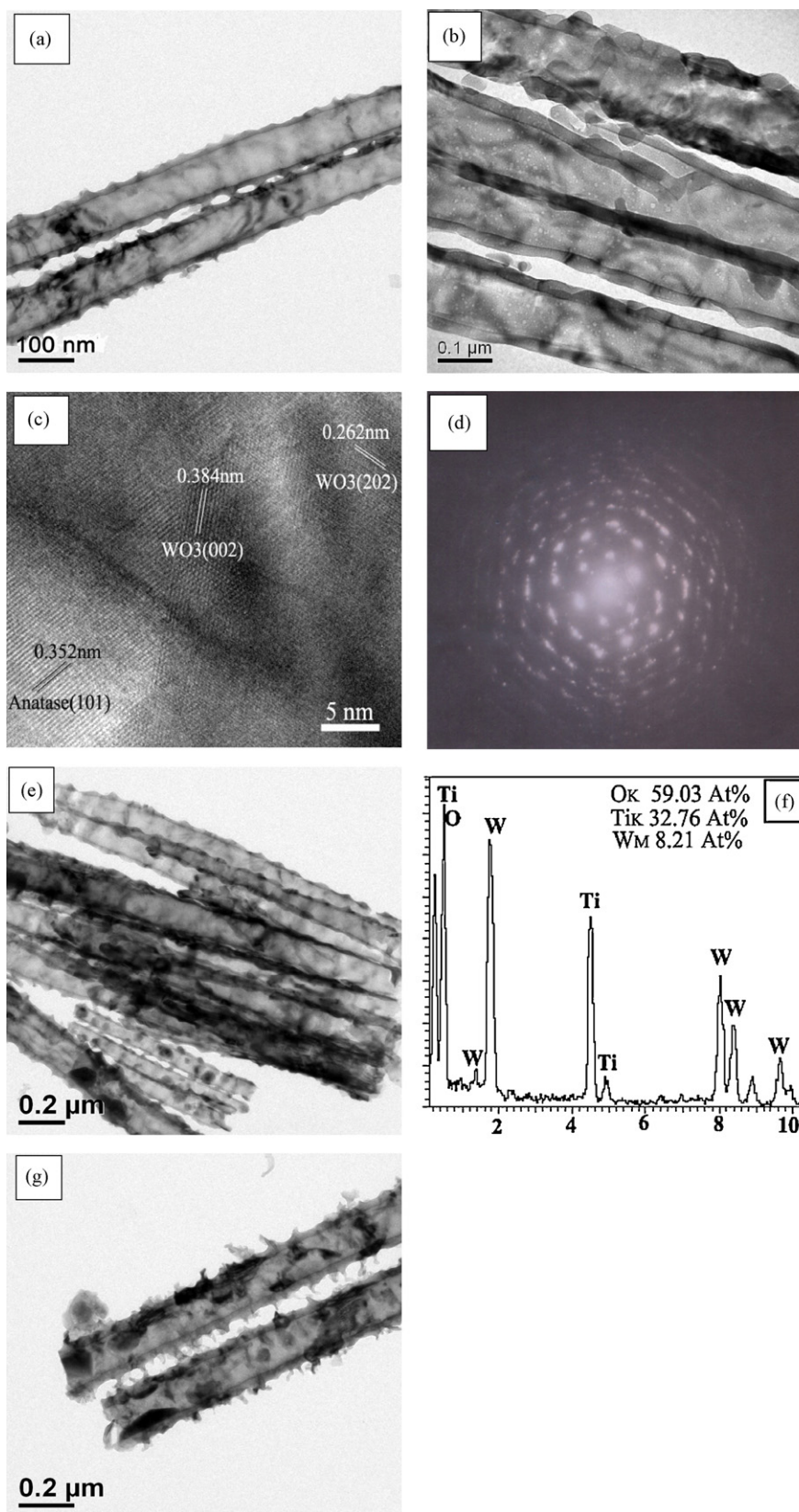


Fig. 3. TEM images of (a) $\text{W}_{0.77\text{at}\%}\text{-TiO}_2$ nanotubes, (b) $\text{W}_{1\text{at}\%}\text{-TiO}_2$ nanotubes, (c) high-resolution TEM image of WO_3/TiO_2 nanotubes, (d) the selected area electron diffraction pattern of the WO_3/TiO_2 specimen, (e) TEM images of $\text{W}_{1.3\text{at}\%}\text{-TiO}_2$ nanotubes, (f) EDS analysis of the particles on TiO_2 nanotubes shown in (e), (g) TEM images of $\text{W}_{2.45\text{at}\%}\text{-TiO}_2$ nanotube with a lot of WO_3 nanoparticles in it.

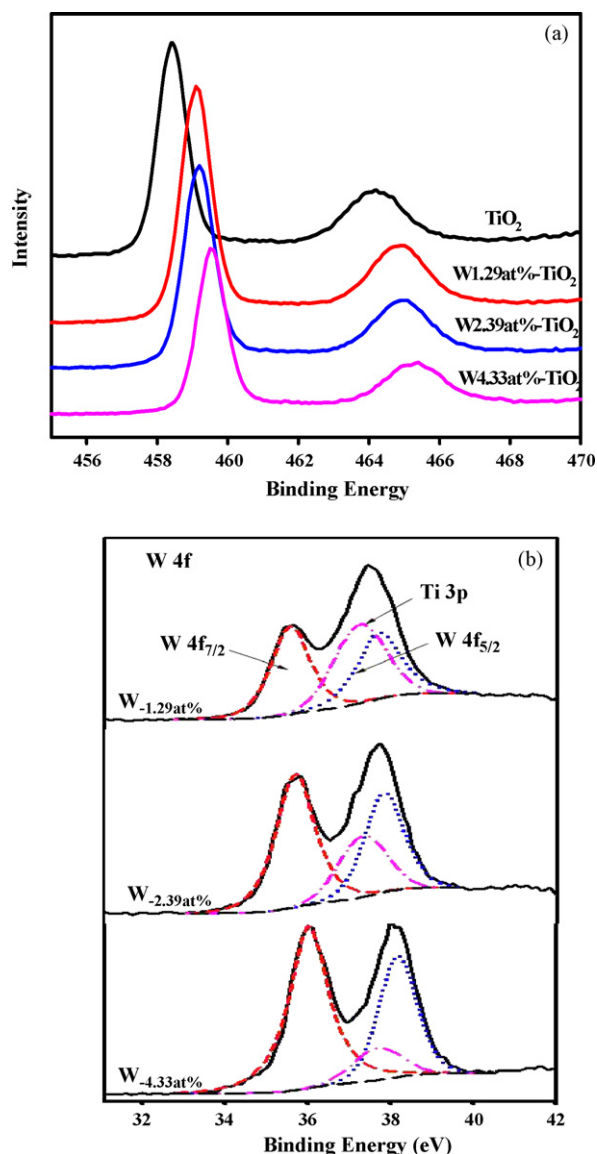


Fig. 4. High-resolution XPS spectra: (a) Ti 2p of TiO_2 NTS and $\text{W}_x\text{-TiO}_2$ NTS, (b) high-resolution XPS spectra and simulated Gaussian line shape W 4f from the $\text{W}_x\text{-TiO}_2$ NTS with increasing W contents ($x = 1.29$ at%, 2.39 at%, 4.33 at%).

analysis of the TiO_2 and WO_3/TiO_2 NT arrays. The Ti $2p_{3/2}$ binding energies assigned to Ti^{4+} increased from 459.1 to 459.53 eV with the increasing W contents. In comparison with the pure TiO_2 [33], the binding energies of Ti 2p shifted to the higher energies, indicating the contraction of the unit cells of TiO_2 due to the W doping [14,34]. These observations suggest the substitution of W for Ti in TiO_2 lattice. Furthermore, the binding energies assigned to W 4f also increased, suggesting the contraction of WO_3 unit cells caused by the substitution of Ti in WO_3 crystals [34]. Moreover, the high-resolution TEM images shown in Fig. 3c depict that the titanium and tungsten oxides are coupled together, indicating that the formation of the solid solution of TiO_2 and WO_3 crystals. The simultaneous contraction in TiO_2 and WO_3 lattices means that the formation of TiO_2 and WO_3 crystals is correlative interplay in the co-crystallization process, resulting from the similar radii of Ti^{4+} and W^{6+} .

Fig. 5 shows the UV–vis absorption spectra of $\text{W}_x\text{-TiO}_2$ and TiO_2 NTS. Compared with the spectrum of undoped TiO_2 , the absorption edge of WO_3 doped TiO_2 shifts to the higher wavelength region due to the low band gap of WO_3 (2.6 eV) [35]. The shift increases with

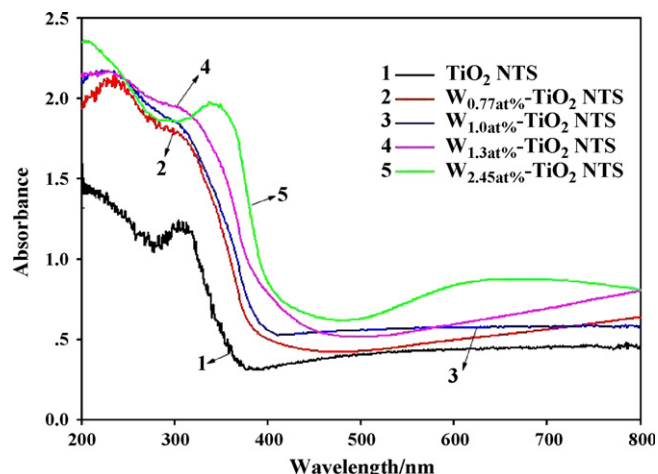


Fig. 5. UV–vis absorption spectra of the $\text{W}_x\text{-TiO}_2$ NTS ($x = 0.77, 1.0, 1.3, 2.45$ at%) and TiO_2 NTS.

the increasing W contents, indicating an extended photo-response into the visible light region resulting from the WO_3 .

The photoelectrochemical behaviors of undoped TiO_2 and $\text{W}_x\text{-TiO}_2$ NTS, in terms of short-circuit currents and open-circuit photovoltage upon illumination of UV–vis light, are presented as [supplementary materials](#). The results show that the $\text{W}_{1.0\text{at\%}}\text{-TiO}_2$ NTS elicit the highest photocurrent and create photogenerated carriers with the longest lifetime. The decreasing photocurrents observed on TiO_2 NTS with W contents higher than 1 at% were caused by the excess WO_3 nanoparticles which attached on the TiO_2 NT walls and served as the recombination centers for the photogenerated electrons and holes. Furthermore, the decrease of the interior space of the WO_3/TiO_2 NTS was also responsible for the decreasing photocurrents. Therefore, the optimum W content in TiO_2 NT arrays would appear to be about 1.0 at% based on the present findings.

3.2. Photocatalytic reduction of Cr(VI) and mechanism investigation

3.2.1. Photocatalytic reduction of Cr(VI) under UV light

Fig. 6 shows the profiles of Cr(VI) reduction under UV light irradiation at an intensity of 25 mW/cm^2 (300–400 nm) under different experimental conditions. The adsorption of Cr(VI) on TiO_2 NTS reaches an equilibrium in 20–30 min, then Cr(VI) is reduced very slowly in the absence of citric acid (Fig. 6, curve 1), as a result of the continuous reduction and reoxidation of chromium species

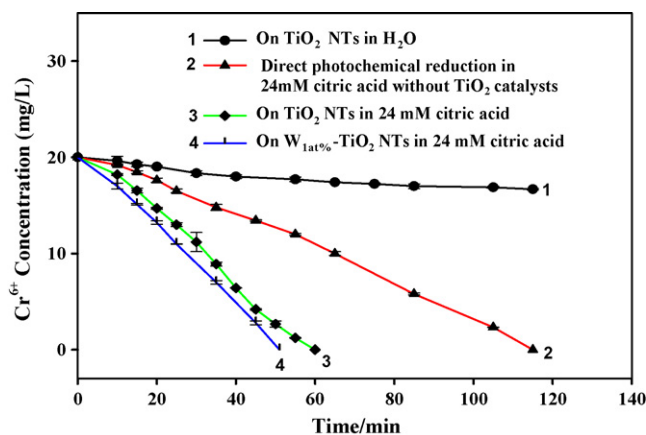
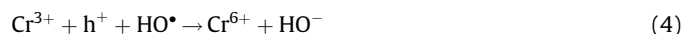
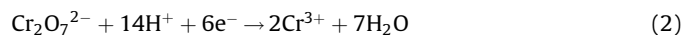


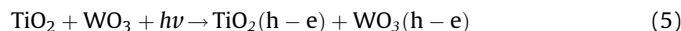
Fig. 6. Photoreduction of Cr^{6+} performed under different conditions when exposed to UV light. $V_{\text{total}} = 20 \text{ mL}$; $S_{\text{catalyst}} = 1 \text{ cm} \times 4 \text{ cm}$; light source: Hg lamp, 25 mW/cm^2 .

by holes and hydroxyl radicals. These recycling reactions can be expressed simply, as follows:



In curve 2 in Fig. 6, significant redox reactions happened between Cr(VI) and citric acid under UV light illumination, with a much faster reduction rate of $43.5 \mu\text{g/L min cm}^2$ in the presence of 24 mM citric acid as compared with the direct photoreduction rate on unmodified TiO_2 NTs (Fig. 6, curve 1). While in dark or under only visible light illumination, no redox reaction occurred between Cr(VI) and citric acid (data not shown). The possible reason is that, upon UV light (300–400 nm) irradiation, the lone pair of electrons of the hydroxyl group on the carboxyl of the citric acid was excited due to its inherent electron rich property. The excited electrons moved into the empty d orbitals of Cr(VI), resulting in the reduction of Cr(VI) and the depletion of the citric acid. However, this phenomenon has been ignored by other researchers [36]. During the photocatalysis, tiny air bubbles were observed on the TiO_2 NT surface. The pH value of the solution changed from 2 to 2.5, indicating that H^+ was depleted in the photocatalysis.

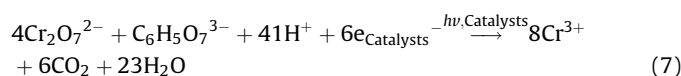
The detailed photocatalytic reactions occurring on WO_3/TiO_2 can be depicted as follows:



The photogenerated electrons are quickly trapped at the NT surface:



where $\text{TiO}_2(e_t)$ and $\text{WO}_3(e_t)$ represents trapped electrons presumably at the Ti^{4+} and W^{6+} sites. As mentioned above, Cr(VI) was reduced through two means including photocatalytic reduction by the photogenerated electrons from TiO_2 photocatalyst and redox between the excited citric acid. The over reaction in this photocatalysis is the reduction of Cr(VI) to Cr(III) and the oxidation of citric acid to CO_2 :



The direct redox reaction rate between Cr(VI) and citric acid, and the Cr(VI) photoreduction rate on unmodified as well as $\text{W}_{1.0\text{at}\%}$ doped TiO_2 NTs in the presence of 24 mM citric acid, are calculated to be 43.5, 83.3, and $98 \mu\text{g/L min cm}^2$, respectively, based on curves 2, 3, and 4, respectively. After deducting the value of the direct reaction between Cr(VI) and citric acid, the net values of the Cr(VI) reduction on unmodified and WO_3 doped TiO_2 NTs are 39.8 and $54.5 \mu\text{g/L min cm}^2$, respectively. Since both WO_3 and TiO_2 can be excited by UV light, the approximately 36.9% enhancement of the photocatalytic activity on WO_3/TiO_2 NTs can be attributed to the increased charge-carrier separating rate and the increasing driving force with fast electron injection resulting from the shift of the TiO_2 conduction band to negative potentials due to the WO_3 doping.

3.2.2. Photocatalytic reduction of Cr(VI) under simulated solar light

In order to further illuminate the effect of the doped WO_3 on the photocatalytic efficiency of TiO_2 , simulated solar light, instead of UV light, was used to excite the photocatalytic reduction of Cr(VI). Fig. 7 shows the typical Cr(VI) reduction curves obtained on $\text{W}_x\text{-TiO}_2$ NTs and unmodified TiO_2 NTs under simulated solar light from a Xe lamp (main wavelengths: 400–700 nm). All of the WO_3 /

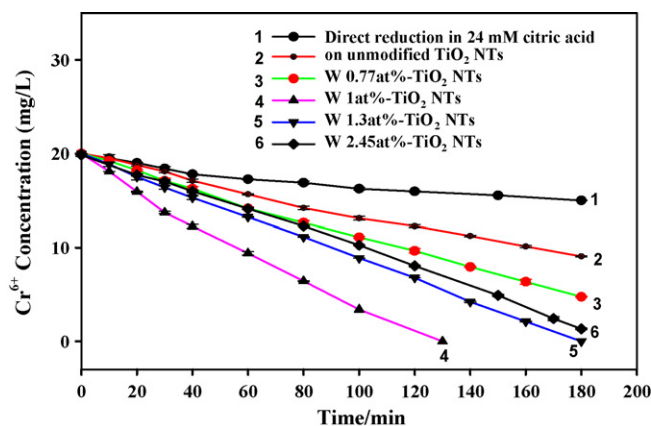


Fig. 7. Photoreduction of Cr^{6+} on $\text{W}_x\text{-TiO}_2$ NTs ($x = 0.77, 1, 1.3, 2.45 \text{ at}\%$) and TiO_2 NTs. $^aV_{\text{total}} = 20 \text{ mL}$; $S_{\text{catalyst}} = 1 \text{ cm} \times 4 \text{ cm}$; light source: Xe lamp, 100 mW/cm^2 .

TiO_2 composite NTs exhibit much higher photocatalytic activities than that of the unmodified TiO_2 NTs. The fastest reduction rate of Cr(VI) on $\text{W}_{1.0\text{at}\%}\text{-TiO}_2$ NTs (curve 4) is $38.5 \mu\text{g/L min cm}^2$ while that on the TiO_2 NTs (curve 2) is $15.2 \mu\text{g/L min cm}^2$. Subtracting the $6.9 \mu\text{g/L min cm}^2$ from the redox between citric acid and Cr(VI) based on curve 1 in Fig. 7, the net reduction rate caused by photogenerated electrons on WO_3/TiO_2 is $31.6 \mu\text{g/L min cm}^2$, which is 2.76 times higher than that ($8.3 \mu\text{g/L min cm}^2$) on TiO_2 . The net improvement of Cr(VI) reduction rate is much higher than the 36.9% improvement obtained under UV light irradiation (Fig. 6), suggesting that the WO_3 doping plays an important role in the absorption of visible light and increasing the probability of charge-carrier separation [37,38].

Obviously, the enhancement of the photoactivity achieved by a photochemical technique without bias potential will be lower than that achieved by a photoelectrochemical technique (shown as supplementary material) where a bias potential of -0.1 V was applied to assist the separation of photogenerated carriers. However, considering the application, photochemical catalysis without applied bias has more practical value.

3.2.3. Influence of pH, ionic strength and temperature on Cr(VI) reduction rate

Fig. 8 depicts the effect of pH (adjusted by H_2SO_4) of the solution on Cr(VI) reduction rates. The pH has a strong influence on the kinetic reduction of Cr(VI). Increasing the acidity until the pH to 1,

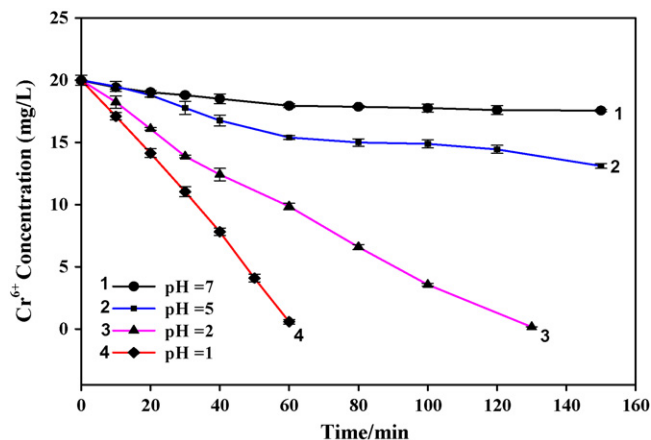


Fig. 8. Influence of solution acidity on the reduction rate of Cr^{6+} in 24 mM citric acid on $\text{W}_{1\text{at}\%}\text{-TiO}_2$ NTs. $^aV_{\text{total}} = 20 \text{ mL}$; $S_{\text{catalyst}} = 1 \text{ cm} \times 4 \text{ cm}$; light source: Xe lamp, 100 mW/cm^2 .

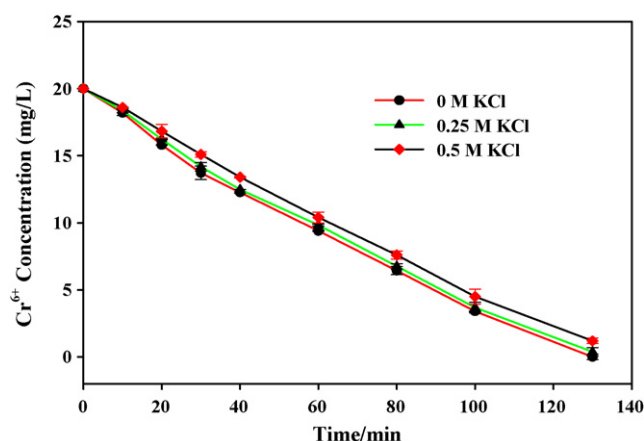


Fig. 9. Influence of ion strength on the reduction rate of Cr^{6+} in 24 mM citric acid on $\text{W}_{1\text{at}\%}\text{-TiO}_2$ NTs. $^aV_{\text{total}} = 20$ mL; $S_{\text{catalyst}} = 1 \text{ cm} \times 4 \text{ cm}$; light source: Xe lamp, 100 mW/cm^2 .

the reduction rates increased. The highest rate of $80.9 \mu\text{g/L min cm}^2$ was obtained at the lowest pH shown as in Fig. 8. It can be seen that the rate of Cr(VI) reduction slows down at higher pH and virtually stops on this time scale at pH 7.

The Nernst equation of the over reaction in this system can be expressed as:

$$\varphi = \varphi^\theta + \frac{0.059}{24} \lg \frac{[\text{Cr}_2\text{O}_7^{2-}]^4 \cdot [\text{C}_6\text{H}_5\text{O}_7^{3-}] \cdot [\text{H}^+]^{41}}{[\text{Cr}^{3+}]^8 \cdot [\text{CO}_2]^6 \cdot [\text{H}_2\text{O}]^{23}} \quad (8)$$

The φ value increased with the increasing concentration of H^+ according to Eq. (8), the equilibrium-reaction would move toward right at increased φ value, meaning that the reduction rate of Cr(VI) would be improved in solution with higher acidity.

Fig. 9 shows the effect of the ionic strength on the reduction rate of Cr(VI) on $\text{W}_{1\text{at}\%}\text{-TiO}_2$ NTs. As is shown in the curves, the reduction rate of Cr(VI) is $38.5 \mu\text{g/L min cm}^2$ in the absence of KCl. The reduction rates in the presence of 0.25 and 0.5 M KCl are 37.7 and $35.9 \mu\text{g/L min cm}^2$, respectively. These observations indicate that the ionic strength has no significant influence on the photocatalytic reduction of Cr(VI) . The slight decrease of the reduction rate might be attributed to the photo-corrosion due to the specific adsorption of Cl^- on the photocatalysts [39,40].

Another determinative factor on influencing the reduction rate of Cr(VI) is temperature. Fig. 10 shows the representative Cr(VI) reduction curves obtained on $\text{W}_x\text{-TiO}_2$ NTs and unmodified TiO_2 NTs under simulated solar light from a Xe lamp without removing the IR

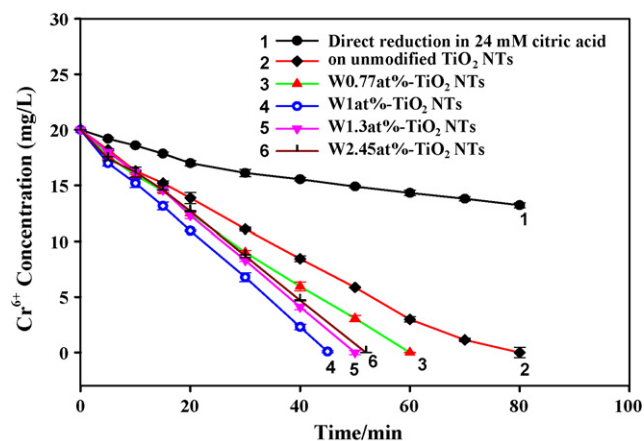


Fig. 10. Influence of temperature on the reduction rate of Cr^{6+} . $^aV_{\text{total}} = 20$ mL; $S_{\text{catalyst}} = 1 \text{ cm} \times 4 \text{ cm}$; light source: Xe lamp with IR irradiation.

Table 2

Reduction rate of Cr(VI) under illumination without/with IR irradiation.

Conditions of Cr(VI) reduction	Xe lamp filtering IR data in Fig. 7 ($\mu\text{g/L min cm}^2$)	Xe lamp with IR data in Fig. 10 ($\mu\text{g/L min cm}^2$)
Direct reduction in citric acid	6.9	21.3
TiO_2 NTs	15.2	62.5
$\text{W}_{0.77\text{at}\%}\text{-TiO}_2$ NTs	21.2	83.3
$\text{W}_{1\text{at}\%}\text{-TiO}_2$ NTs	38.5	110.6
$\text{W}_{1.3\text{at}\%}\text{-TiO}_2$ NTs	27.8	100
$\text{W}_{2.45\text{at}\%}\text{-TiO}_2$ NTs	25.7	96.2

irradiation. The reduction rate of Cr(VI) was significantly enhanced under the assistance of IR light which heated up the treated solution to 35°C in 30 min. Table 2 summarizes the reduction rates under room temperature of Cr(VI) based on Figs. 7 and 10. Subtracting the reduction rate of $21.3 \mu\text{g/L min cm}^2$ resulting from the direct redox reaction with citric acid under illumination, the fastest reduction rate of Cr(VI) is $89.3 \mu\text{g/L min cm}^2$. The high temperature accelerates the random thermal motion of the molecules, increasing the entropy of the photocatalytic system and facilitating the Cr(VI) reduction. The higher the temperature, the faster the reduction rate of Cr(VI) . Since the light source from Xe lamp with IR irradiation is similar to the natural solar light, the fast Cr(VI) reduction rate suggests that the WO_3/TiO_2 NT arrays are promising functional materials for the Cr(VI) removal in practical application with making full use of the natural solar energy.

4. Conclusion

This work reports the Cr(VI) photocatalytic reduction behaviors on WO_3 doped TiO_2 NT arrays in the presence of citric acid, which serves as both a donor scavenger and a redox reagent in the photocatalytic process. The fabricated WO_3/TiO_2 NT arrays were composed of crystalline WO_3 and TiO_2 and showed extended absorption spectra in the visible light region. The highest photoreduction efficiency of Cr(VI) was obtained on the WO_3/TiO_2 NTs with 1.0 at% W content. Since the WO_3/TiO_2 NT arrays can be easily removed and replaced after the photocatalytic reaction, avoiding the filtration step after photoreaction or the immobilizing process required for photocatalyst particles, the operation in the photoreactor becomes much easier from an engineering point of view. The unique organization and the high photocatalytic efficiency of WO_3/TiO_2 NT arrays also allow a number of potential applications in environmental remediation.

Acknowledgments

We thank Shaohuan Liu for assistance and discussion in the XPS data. This work was supported by the National Science Foundation for Distinguished Young Scholars under Grant 50725825, the National Basic Research Program of China, 2009CB421601, the Natural Science Foundation of Hunan Province, China under Grant 08JJ3113, the National Science Foundation of China under Grant No. 50878079 and the Innovation Project in Postgraduation Education for Excellent Doctors No. 521218019.

Appendix A. Supplementary data

Supplementary data associated with this article can be found, in the online version, at doi:10.1016/j.apcatb.2009.11.002.

References

- [1] R.J. Kieber, J.D. Willey, S.D. Zvalaren, Environ. Sci. Technol. 36 (2002) 5321–5327.
- [2] J.J. Testa, M.A. Grela, M.I. Litter, Environ. Sci. Technol. 38 (2004) 1589–1594.

- [3] P. Mohapatra, S. Samantaray, K.M. Parida, J. Photochem. Photobiol. A Chem. 170 (2005) 189–194.
- [4] H.B. Yu, S. Chen, X. Quan, H.M. Zhao, Y.B. Zhang, Environ. Sci. Technol. 42 (2008) 3791–3796.
- [5] D.P. Das, K. Parida, B.R. De, J. Mol. Catal. A: Chem. 245 (2006) 217–224.
- [6] G.K. Mor, O.K. Varghese, R.H.T. Wilke, S. Sharma, K. Shankar, T.J. Latempa, K.S. Choi, C.A. Grimes, Nano Lett. 8 (2008) 1906–1911.
- [7] G.K. Mor, H.E. Prakasam, O.K. Varghese, K. Shanker, C.A. Grimes, Nano Lett. 7 (2007) 2356–2364.
- [8] Z. Jiang, F. Yang, N.J. Luo, B.T.T. Chu, D. Sun, H.H. Shi, T.C. Xiao, P. Edwards, Chem. Commun. 47 (2008) 6372–6374.
- [9] S.Y. Kuang, L.X. Yang, S.L. Luo, Q.Y. Cai, Appl. Surf. Sci. 255 (2009) 7385–7388.
- [10] A. Kongkanand, K. Tvrđy, K. Takechi, M. Kuno, P.V. Kamat, J. Am. Chem. Soc. 130 (2008) 4007–4015.
- [11] Y. Bessekhouad, D. Robert, J.-V. Weber, Catal. Today 101 (2005) 315–321.
- [12] C. Bechinger, G. Oefinger, S. Herminghaus, P.J. Leiderer, Appl. Phys. 74 (1993) 4527–4533.
- [13] T. Tatsuma, S. Saitoh, Y. Ohko, A. Fujishima, Chem. Mater. 13 (2001) 2838–2842.
- [14] W.B. Su, J.F. Wang, H.C. Chen, W.X. Wang, G.Z. Zang, Mater. Sci. Eng. B 99 (2003) 461–464.
- [15] M. Kobayashi, K. Katsunori, Appl. Catal. B: Environ. 72 (2007) 253–261.
- [16] V. Keller, P. Bernhardt, F. Garin, J. Catal. 215 (2003) 129–138.
- [17] K.K. Akurati, A. Vital, J.-P. Dellmann, K. Michalow, T. Graule, D. Ferri, A. Baiker, Appl. Catal. B Environ. 79 (2008) 53–62.
- [18] H. Shinguu, M.M.H. Bhuiyan, T. Ikegami, K. Ebihara, Thin Solid Films 506–507 (2006) 111–114.
- [19] J. Georjeva, S. Armanov, E. Valova, I. Poullos, S. Sotiropoulos, Electrochem. Commun. 9 (2007) 365–370.
- [20] C.-S. Hsu, C.-K. Lin, C.-C. Chan, C.-C. Chang, C.-Y. Tsay, Thin Solid Films 494 (2006) 228–233.
- [21] G.K. Mor, K. Shankar, M. Paulose, O.K. Varghese, C.A. Grimes, Nano Lett. 6 (2006) 215–218.
- [22] G.K. Mor, M. Paulose, O.K. Varghese, C.A. Grimes, Nano Lett. 5 (2005) 191–195.
- [23] K. Shankar, J. Bandara, M. Paulose, H. Wietasch, O.K. Varghese, G.K. Mor, T.J. Latempa, M. Thelakkat, C.A. Grimes, Nano Lett. 8 (2008) 1654–1659.
- [24] J. Lin, R.L. Zong, M. Zhou, Y.F. Zhu, Appl. Catal. B Environ. 89 (2009) 425–453.
- [25] L.X. Yang, S.L. Luo, S.H. Liu, Q.Y. Cai, J. Phys. Chem. C 112 (2008) 8939–8943.
- [26] Y.B. Liu, B.X. Zhou, J. Bai, J.H. Li, J.L. Zhang, Q. Zheng, X.Y. Zhu, W.M. Cai, Appl. Catal. B Environ. 89 (2009) 142–148.
- [27] K. Onoda, S. Yoshikawa, Appl. Catal. B Environ. 80 (2008) 277–285.
- [28] N. Quici, M.E. Morgada, R.T. Gettar, M. Bolte, M.I. Litter, Appl. Catal. B Environ. 71 (2007) 117–124.
- [29] L.M. Wang, Nan Wang, L.H. Zhu, H.W. Yu, H.Q. Tang, J. Hazard. Mater. 152 (2008) 93–99.
- [30] T. Kudo, Nature 312 (1984) 537–538.
- [31] J.H. Pan, W.I. Lee, Chem. Mater. 18 (2006) 847–853.
- [32] D. Gogova, K. Gesheva, A. Kakanakova-Georgieva, M. Surtchev, Eur. Phys. J. AP 11 (2000) 167–174.
- [33] J. Abad, O. Bohme, E. Roman, Surf. Sci. 549 (2004) 134–142.
- [34] R.G. Palgrave, I.P. Parkin, J. Mater. Chem. 14 (2004) 2864–2867.
- [35] F.J. Himpsel, J.F. Morar, F.R. McFeely, R. Pollak, G. Hollinger, Phys. Rev. B30 (1984) 7236–7241.
- [36] J.M. Meichtry, M. Brusa, G. Mailhot, M.A. Grela, M.I. Litter, Appl. Catal. B Environ. 71 (2007) 101–107.
- [37] X.Z. Li, F.B. Li, C.L. Yang, W.K. Ge, J. Photochem. Photobiol. A Chem. 141 (2001) 209–217.
- [38] Y.T. Kwon, K.Y. Song, W.I. Lee, G.J. Choi, Y.R. Do, J. Catal. 191 (2000) 192–199.
- [39] K.H. Wang, Y.H. Hsieh, C.H. Wu, C.Y. Chang, Chemosphere 40 (2000) 389–394.
- [40] A. Piscopo, D. Robert, J.V. Webe, Appl. Catal. B Environ. 35 (2001) 117–124.